Open Archive Toulouse Archive Ouverte (OATAO)

OATAO is an open access repository that collects the work of some Toulouse researchers and makes it freely available over the web where possible.

This is an author's version published in: https://oatao.univ-toulouse.fr/26850

Official URL : https://doi.org/10.1109/TNS.2020.3003451

To cite this version :

Le Roch, Alexandre and Virmontois, Cédric and Paillet, Philippe and Belloir, Jean-Marc and Rizzolo, Serena and Marcelot, Olivier and Dewitte, Hugo and Van Uffelen, Marco and Casellas, Laura Mont and Magnan, Pierre and Goiffon, Vincent Phosphorus Versus Arsenic: Role of the Photodiode Doping Element in CMOS Image Sensor Radiation-Induced Dark Current and Random Telegraph Signal. (2020) IEEE Transactions on Nuclear Science, 67 (7). 1241-1250. ISSN 0018-9499

Any correspondence concerning this service should be sent to the repository administrator: tech-oatao@listes-diff.inp-toulouse.fr

Phosphorus Versus Arsenic: Role of the Photodiode Doping Element in CMOS Image Sensor Radiation-Induced Dark Current and Random Telegraph Signal

Alexandre Le Roch, *Graduate Student Member, IEEE*, Cédric Virmontois, *Senior Member, IEEE*, Philippe Paillet, *Fellow, IEEE*, Jean-Marc Belloir, *Member, IEEE*, Serena Rizzolo, *Member, IEEE*, Olivier Marcelot, *Member, IEEE*, Hugo Dewitte, *Student Member, IEEE*, Marco Van Uffelen, *Senior Member, IEEE*, Laura Mont Casellas, Pierre Magnan, *Member, IEEE*, and Vincent Goiffon, *Senior Member, IEEE*

***Abstract*— This work the role of the phosphorus doping element in the radiation-induced dark current in a CMOS image sensor (CIS) photodiode. The neutron and proton irradiations on shallow arsenic-based photodiode CISs and deep phosphorus-based photodiodes CISs have been performed. The results highlight the applicability of the same dark current increase and random telegraph signal (RTS) models. Already verified on other photodiode structures, these results further extend the universality of these analytic tools. Moreover, it emphasizes that the phosphorus element does not play a significant role either in the radiation-induced dark current increase or in the dark current RTS. The results on RTS after annealing reveal the same recovery dynamic than those already observed in irradiated image sensors, suggesting that the phosphorus element does not play a significant role after annealing. Therefore, this work is a piece of experimental evidence supporting the idea that RTS induced by displacement damage is principally due to defect clusters mainly constituted of intrinsic silicon defects such as clusters of vacancies and interstitials.**

***Index Terms*— Annealing, arsenic, cluster, CMOS image sensor (CIS), dark current, deep photodiode, displacement damage dose (DDD), E-center, electric field enhancement (EFE), neutron, phosphorus, proton, random telegraph signal (RTS), shallow photodiode, total ionizing dose (TID).**

I. Introduction

Doping elements considered in imaging technologies including charge-coupled device (CCD) and CMOS image sensor (CIS) always result from the final shape of the p-n junction to achieve. Usually, advanced imaging technologies use ion implantation processes to monitor the doping profile. The implantation parameters are, therefore, a tradeoff between the ion beam energy, the elements considered, as well as their thermally assisted diffusivity into the silicon. The last annealing phase results in the final p-n junction structure. Even though the vast majority of CIS photodiodes are based on n-type implantation into p-type epitaxial layer, the doping elements present into the photodiode are difficult to identify since it is related to the foundry intellectual property. Without this information, the effects of such doping elements or impurities on the dark current are even more complicated to discuss since photodiodes often present several elements for doping profile optimization purposes.

Radiation exposure makes the role of doping elements and impurities in imager dark current even more complicated to investigate. Indeed, when exposed to radiation, incident energetic particles traveling through the silicon lose their energy to ionizing and nonionizing processes. The result of this energy loss is the production of electron–hole pairs called ionization (ionizing process) and displaced silicon atoms called displacement damage (nonionizing process). Permanent degradations related to the ionizing energy loss mostly refer to oxide charge trapping and Si/SiO_2 interface defects [1]. Differently, permanent degradation related to the nonionizing energy loss (NIEL) mostly refers to bulk damage into the silicon resulting from the creation of vacancies and interstitials known as Frenkel pairs. Following Frenkel pairs creation, local groupings of vacancies and interstitials may occur and additional types of defects can be created when vacancies and interstitials are adjacent to impurity or doping atoms. The resulting defects are called defect–impurity complexes [2]. Radiation-induced charge trapping and Si/SiO_2 interface defects creation mostly lie in the oxide and the Si/SiO_2 interface quality. Therefore, only bulk defects are susceptible to interact with impurities or doping elements into the silicon and could impact the dark current. Ionizing and displacement damage are measured by the total ionizing dose (TID) and the displacement damage dose (DDD). In the case of neutron

Alexandre Le Roch, Serena Rizzolo, Olivier Marcelot, Hugo Dewitte, Pierre Magnan, and Vincent Goiffon are with ISAE-SUPAERO, Université de Toulouse, 31055 Toulouse, France (e-mail: alexandre.le-roch@isae-supaero.fr).

Cédric Virmontois and Jean-Marc Belloir are with the Centre National d'Etudes Spatiales (CNES), 31400 Toulouse, France.

Philippe Paillet is with CEA, DAM, DIF, 91297 Arpajon, France.

Marco Van Uffelen and Laura Mont Casellas are with Fusion for Energy, 08019 Barcelona, Spain.

Digital Object Identifier 10.1109/TNS.2020.3003451

irradiations, a large majority of bulk defects are created by displacement. When located in depleted regions, those defects act as generation centers (also called Shockley Read Hall centers [3]), leading to a dark current increase. Depending on the neutron fluence, indirect ionization coming from displaced silicon ions might lead to a nonnegligible TID. In the case of proton irradiations, both ionizing deposition and displacement damage are significant. Hence, both interface defects and bulk defects are created and participate in the dark current increase when located in the depleted regions. However, as explained before, only bulk defects are susceptible to interact with impurities or doping elements into the silicon, and the present study focus on displacement damage.

In the literature, several articles discussed the role of the radiation-induced bulk defects in the imager dark current. On the one hand, based on the similarity of the damage factor for a wide variety of silicon devices, Srour and Lo [4] suggested that the dark current after irradiation is more likely caused by clustered vacancies and interstitials rather than isolated defects related to impurity or doping element. On the other hand, it is known from the literature that annealing occurs in all irradiated silicon-based devices. Following irradiation, the first annealing behavior is a significant short-term annealing of the dark current observed in CCD in [5] and [6] and in CIS in [7]. High-temperature annealing behavior until 150 °C reported in irradiated CCD in [8] seems to eliminate the role of the divacancies which are supposed to anneal at a higher temperature [9]. Hence, as supported in [10], annealing behavior also suggests that the dark current in irradiated silicon devices is more likely caused by clustered vacancies and interstitials susceptible to anneal at temperatures below 150 °C. These results have proved to be consistent with those obtained by dark current spectroscopy (DCS) on irradiated CIS in [11]–[13]. In these studies, annealing temperatures until 300 °C allowed to point out the contribution of the divacancies in the total dark current distribution but also highlighted that many other defects still participate in the overall dark current. To summarize, even if the identification of bulk defects related to impurities and/or doping elements can be revealed in the total dark current contribution either by DCS in imagers or by other techniques such as electron paramagnetic resonance (EPR) [14]–[16] and deep-level transient spectroscopy (DLTS) [17] in single structures, the origin of the dark current in irradiated silicon devices seems to be mainly driven by a wide variety of clustered intrinsic defects (i.e., interstitial and vacancy) susceptible to anneal in the temperature range of 100 °C. Finally, annealing of displacement damage is a complex process with various regimes and dependencies. In particular, when high displacement damage is concerned, the annealing shows a damage reduction over a broad range of temperatures which does not match with specific isolated defects or simple defect complexes but rather with amorphous inclusion as supported in [18].

In addition to the overall radiation-induced dark current increase in imagers, the dark current random telegraph signal (RTS) also degrades the imager's performances. Moreover, first observed in irradiated CCD in [19]–[21], this discreet and random fluctuation of the dark current initiates a new

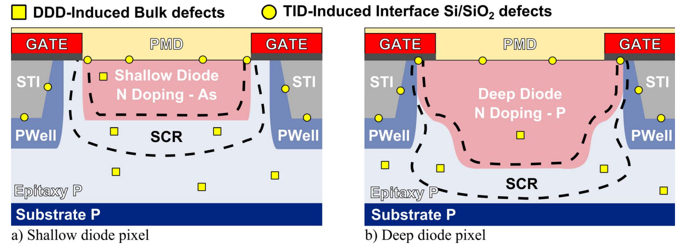

Fig. 1. Cross sections of the two considered pixels. (a) Shallow arsenic-based implantation. (b) Deep phosphorus-based implantation. Radiation-induced defects related to displacement (bulk defects) and ionizing dose (interface defects) are reported by the yellow dots in both structures.

vision of metastable semiconductor defects. The origin of this RTS is still under investigation in the community and raises a significant interest in the understanding of the physical phenomena involved in defects metastability in silicon. In irradiated CCD, Hopkins and Hopkinson [21] suggested the role of vacancy clusters as well as the hypothetical role of the phosphorus–vacancy (P–V) center (also referred to as E-center) in the RTS behavior [22]. Later, Nuns *et al.* [23] also proposed the metastability of the P–V center as responsible for the RTS in irradiated CCD. Following CCD, Hopkinson *et al.* [24] highlighted the existence of RTS in CIS and suggested the prevalence of intrinsic defects associated with cluster damage, also discussed in [25] and [18], [26], [27], rather than isolated defects which seem inconsistent with the clustering hypothesis for multilevel RTS. More recently, the P–V center has also been suggested to be responsible for the RTS behavior in single-photon avalanche diode (SPAD) [28]. Today, the role of the phosphorus element in the RTS behavior observed in irradiated silicon devices is still discussed.

Finally, further investigations aiming to determine the role of the phosphorus both in the radiation-induced dark current and the RTS are crucial to pushing forward the knowledge on defects creation in silicon-based devices. The origin of the RTS in irradiated silicon devices is not clearly determined yet, and the role of the doping element, specifically the phosphorus, is essential to foresee future RTS mitigation techniques.

II. Experimental Details

This study investigates the role of the photodiode doping element in the radiation-induced dark current increase and the RTS maximum transition amplitude (i.e., maximum amplitude between two dark current levels) after the 50-MeV proton and 22-MeV neutron irradiations. Impinging particles (i.e., neutrons and protons) have been chosen to extend the investigation to different irradiation conditions leading to displacement damages. The comparisons between proton and neutron irradiations in terms of dark current increase are based on the same deposited DDD. For the considered energies, the NIEL for protons and neutrons are quite similar reaching 4.0 $\text{keV} \cdot \text{cm}^2\ \text{g}^{-1}$ with 10% uncertainty. Moreover, following the NIEL scaling approach [26], the DDD-induced dark currents are expected to be similar between proton and neutron irradiations sharing the same DDD.

Two identical 3-transistor (3T) CISs sharing the same layout design have been used in this study. The only difference between the two CIS is the photodiode implantation which

TABLE I

DOPING IMPLANT CHARACTERISTICS

Implant Characteristics	Lot 1	Lot2
Sensor Reference	A/B/C/D/E	F/G/H/I/J
Doping Element	Arsenic	Phosphorus
Implant Type	Shallow	Deep
Implant Depth (μm)	0.55	1.5
CVF ($\mu V/e^-$)	12.6	7.2
Depletion Volume (μm^3)	44	56

TABLE II

IRRADIATION PARAMETERS

CIS	Particle	Fluence (cm^{-2})	DDD ($TeV.g^{-1}$)	TID ($krad(SiO_2)$)
A/F	Proton 50 MeV	1×10^{10}	40	1.65
B/G	Proton 50 MeV	1×10^{11}	400	16.5
C/H	Neutron 22 MeV	1×10^{10}	40	1×10^{-2}
D/I	Neutron 22 MeV	1×10^{11}	400	1×10^{-1}
E/J	Neutron 22 MeV	1×10^{12}	4000	1

is either based on shallow arsenic-based implantation or deep phosphorus-based implantation. The CISs under test are manufactured in a commercially available 180-nm CMOS imaging technology and comprise a 128×128 pixel array with three transistors per pixel (i.e., 3T CIS) and a 10 μm pitch. Each tested CIS is mounted on the PGA84 ceramic package. Fig. 1 illustrates the considered shallow arsenic-based photodiode pixel and the deep phosphorus-based photodiode pixel. In the same figure, the interface defects induced by the TID and the bulk defects induced by the DDD are shown. Both structures are radiation hardened by design and present an enclosed gate surrounding the photodiode implantation. Following the TCAD simulation discussed in Section III-B.3, the photodiode implantation characteristics are summarized in Table I. The charge to voltage factor (CVF) relies on the mean-variance measurements under illumination [29].

Four CISs have been irradiated at room temperature with a 50-MeV proton beam using two fluences and six CISs have been irradiated with a 22-MeV neutron beam at three fluences at "Université Catholique de Louvain" in Leuven, Belgium. Uncertainty on the fluences is less than 10%. Whereas the proton beam can be considered as mono-energetic, the neutron beam is a spectrum centered on 22 MeV and spreads from 10 to 40 MeV. Each fluence has been performed simultaneously on two CISs coming from different lots. The CISs have been directly exposed to the proton or neutron beam with no shielding and with all the pins grounded. The irradiation parameters are summarized in Table II.

All the measurements have been performed in the dark in a temperature-controlled chamber at 22 °C after four weeks of room temperature annealing. The dark current measurements use six integration times from a few milliseconds to 1 s. Each image attributed to a given integration time is built from the average image of ten acquisitions to reduce the temporal noise. The dark current of each pixel I_{dark} is computed as the slope of the output voltage as a function of the integration time T_{int} using the CVF

$$I_{\text{dark}} = \frac{\Delta \text{Signal}}{\Delta T_{\text{int}}} \times \frac{1}{\text{CVF}}. \quad (1)$$

During the integration, while thermally generated charges are collected in the photodiode, the gate is biased in its accumulation regime at -0.2 V to confine the space charge region (SCR) and prevent the collection of thermally generated charges from the gate oxide interface defects minimizing the TID dark current contribution. The dark current RTS analysis method lies in the measurement of the per-pixel dark current evolution with time. It uses a rising edge detection algorithm over 15 000 images with a 1-s sampling time as introduced in [30] and further developed in [31].

III. DARK CURRENT DISTRIBUTIONS

A. Dark Current Increase Distribution Model

The dark current increase in one pixel attributed to displacement damage is labeled $\Delta I_{\text{dark}_{\text{DDD}}}$. Using the probability density function (PDF) to study the whole population of pixels over the sensor array, the global distribution is labeled $f_{\Delta I_{\text{dark}_{\text{DDD}}}}(x)$, with x the dark current. This PDF is built from the convolution of several elementary exponential PDF according to what is reported in [32] and [33]. The validity of this model, whose input parameters are the considered depleted volume and the deposited DDD, has been proved on several CIS technologies and irradiation parameters [12], [34]. To account for the TID contribution in the dark current increase distribution, the PDF model labeled $f_{\Delta I_{\text{dark}_{\text{TID}}}}(x)$ is considered. This PDF is comparable to a normal distribution, as reported in many irradiated imagers [35] and can be seen as a Gaussian-based PDF whose inputs parameters are the experimental mean and standard deviation (i.e., shot noise) of the dark current [36]. Usually, experimental data discrepancy from the Gaussian-based TID model can be interpreted as an electric field effect and tend to hint a Gamma-based distribution whose input parameters are the shape parameter and the scale parameter. This distortion of the dark current distribution has been explored following other irradiation parameters in [10], [19], and [37]. Finally, the mixed dark current increase $\Delta I_{\text{dark}_{\text{TID+DDD}}}$ can be expressed as the sum of the DDD and the TID dark current increase

$$\Delta I_{\text{dark}} = \Delta I_{\text{dark}_{\text{DDD}}} + \Delta I_{\text{dark}_{\text{TID}}}. \quad (2)$$

The mixed dark current increase distribution is built from the convolution of the two PDF models and expressed as

$$f_{\Delta I_{\text{dark}}}(x) = f_{\Delta I_{\text{dark}_{\text{TID}}}}(x) * f_{\Delta I_{\text{dark}_{\text{DDD}}}}(x). \quad (3)$$

The final model introduced in (3) accounts both for the TID and the DDD dark current increase. Since the DDD contribution can be estimated from the total dark current after the proton and neutron irradiations, a comparison of the DDD contributions can be performed to highlight the role of the doping element. For each sensor, the per-pixel dark current increase is computed from the dark current value after irradiation minus the preirradiation dark current value. Then,

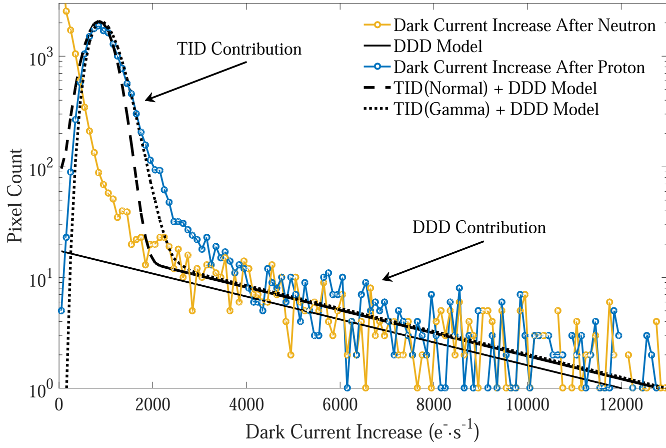

Fig. 2. Dark current increase distributions in the shallow arsenic-based photodiode CIS after $\phi = 10^{10}\text{cm}^{-2}$ proton and neutron irradiations.

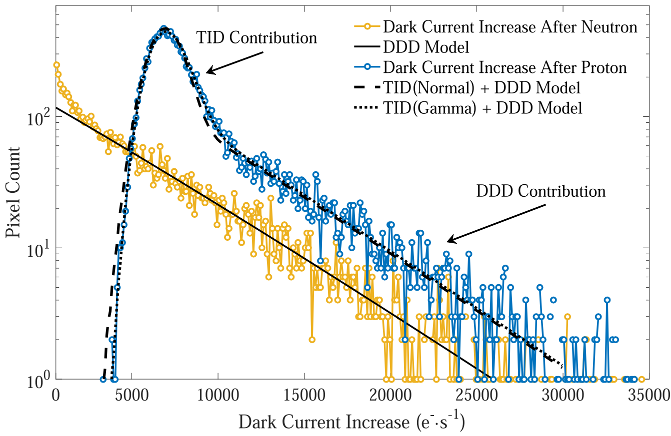

Fig. 3. Dark current increase distributions in the shallow arsenic-based photodiode CIS after $\phi = 10^{11}\text{cm}^{-2}$ proton and neutron irradiations.

the dark current increase distribution over the sensor array is compared to the prediction model. Since the CIS photodiodes in lot 1 and lot 2 do not share the same depleted volume, the comparison of experimental data with the prediction model (based on the considered depletion volume) allows to compare the two CISs. Therefore, any discrepancy from the model can be interpreted as proper to the CIS.

B. Dark Current Distribution Analysis

1) Shallow Arsenic-Based Photodiode: The dark current distributions for the shallow arsenic-based photodiode CIS following the neutron and proton irradiations are reported in Figs. 2 and 3. Fig. 2 shows the dark current increase distributions and the prediction models at the lowest fluence $\phi = 10^{10}\text{cm}^{-2}$. Fig. 3 shows the dark current increase distributions and the prediction models at higher fluence $\phi = 10^{11}\text{cm}^{-2}$.

After the neutron irradiations, the dark current increase distributions reveal a continuously decreasing dark current tail, increasing with the fluence as shown in Figs. 2 and 3. These results are commonly reported in 3T CIS after the neutron irradiation [35]. At the lowest fluence, in Fig. 2, the low dark current increase contribution until 2000 $e^- \cdot s^{-1}$ is due to the indirect TID contribution. This contribution becomes negligible at higher fluence when the dark current

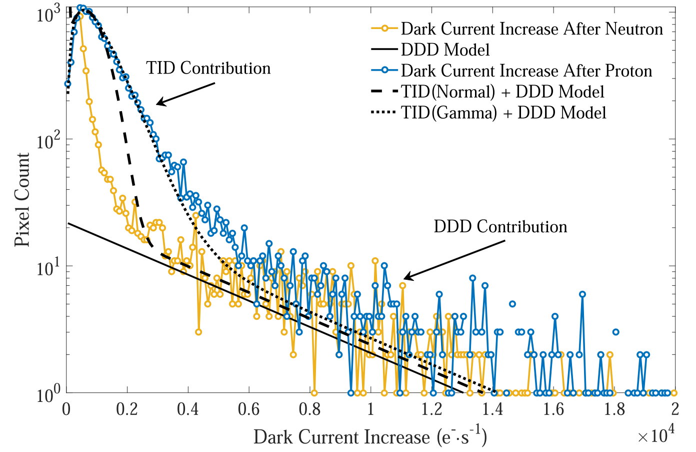

Fig. 4. Dark current increase distributions in the deep phosphorus-based photodiode CIS after $\phi = 10^{10}\text{cm}^{-2}$ proton and neutron irradiations.

increase attributed to the DDD becomes more significant as visible in Fig. 3. At these neutron fluences, no Gaussian TID contribution can be outlined from the distributions showing that the DDD is the dominant contribution in the dark current increase. Finally, experimental data after the 22-MeV neutron irradiations are in good agreement with the dark current increase prediction model for the two considered fluences.

After the proton irradiations, the dark current increase distributions reveal a spike containing the majority of the pixels and a continuously decreasing dark current tail. These results are commonly reported in 3T CIS after the proton irradiation [35]. Whereas the main spike results from the TID contribution, the DDD contribution affects a smaller population of pixels and is visible as a typical continuous dark current tail as seen after the neutron irradiations. The dark current increase shift observed between the neutron and proton distributions increases with the deposited TID as visible in Figs. 2 and 3. This shift is due to the proton TID contribution. Finally, experimental data after the 50-MeV proton irradiations are in good agreement with the dark current increase prediction model for the two considered fluences.

The results after the irradiations highlight that the prediction dark current increase model is applicable for this shallow arsenic-based photodiode CIS. Usually, experimental data discrepancy from the Gaussian-based TID model can be interpreted as an electric field effect and tend to hint a Gamma-based distribution. Comparing the two TID models after proton irradiations, no significant electric field effect can be pointed out in this CIS.

2) Deep Phosphorus-Based Photodiode: The dark current distributions for the deep phosphorus-based photodiode CIS following the neutron and proton irradiations are reported in Figs. 4 and 5. Fig. 4 shows the dark current increase distributions and the prediction models at the lowest fluence $\phi = 10^{10}\text{cm}^{-2}$. Fig. 5 shows the dark current increase distributions and the prediction models at higher fluence $\phi = 10^{11}\text{cm}^{-2}$.

After the neutron irradiations, the dark current increase distributions hint a similar continuously decreasing dark current tail than the shallow arsenic-based photodiode. Moreover, a similar indirect TID contribution resulting in a

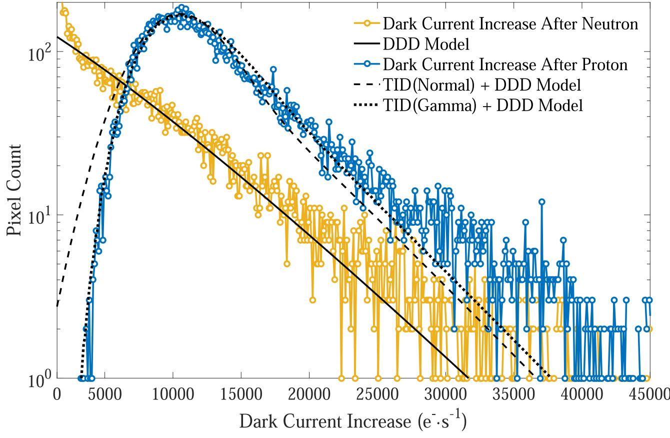

Fig. 5. Dark current increase distributions in the deep phosphorus-based photodiode CIS after $\phi = 10^{11}\text{cm}^{-2}$ proton and neutron irradiations.

low dark current increase is observed at the lowest fluence and becomes negligible at higher fluence. The DDD-induced dark current tail increases the deposited DDD as shown in Figs. 4 and 5 and are in good agreement with the dark current increase prediction model. Finally, experimental data after the 22-MeV neutron irradiations are in good agreement with the prediction model for the two fluences.

After the $\phi = 10^{10}\text{cm}^{-2}$ proton irradiation, the dark current increase distribution in Fig. 4 reveals a spike containing the majority of the pixels and a continuously decreasing dark current tail as observed for the shallow arsenic-based photodiode after the same irradiation. However, the Gamma-based dark current distribution model better fits the experimental data suggesting the existence of electric field enhancement (EFE). Considering the displacement damage, its contribution is visible in the dark current increase tail and seems in reasonably good agreement with the prediction model. After the $\phi = 10^{11}\text{cm}^{-2}$ proton irradiation, the dark current increase distribution in Fig. 5 reveals a spike, related to the TID, but the previously mentioned dark current tail is not as evident as seen in the shallow arsenic-based photodiode after the same irradiation. The EFE highlighted after the lowest fluence seems more significant at higher fluence. As this discrepancy from the prediction model is not observed in the case of neutron irradiations with lower TID, it is probably linked to the high TID deposition.

Finally, results after neutron irradiations confirm that the dark current increase prediction model is applicable for this deep phosphorus-based photodiode CIS. However, the proton irradiation reveals a discrepancy from the Gaussian-based TID model, preventing a clear identification of the DDD contribution. This discrepancy can be explained by an electric field effect enhancing the TID-induced interface defects generation rate, which is not present in the shallow arsenic-based photodiode CIS.

3) Role of the Electric Field: To verify the existence of a high-magnitude electric field region in the deep phosphorus-based photodiode which could result in an EFE of the dark current increase, TCAD simulations have been performed on the two CIS structures. The doping distribution is computed from secondary ion mass spectrometry (SIMS) profiles employing the Sentaurus Structure Editor tool and the dimensions are based on the CIS design developed at ISAE-SUPAERO in the image sensor research team. The doping level of the epitaxy is about $N_{A_{\text{epi}}} \approx 10^{15}\text{cm}^{-3}$ and reaches $N_{D_{\text{PD}}} \approx 10^{17}\text{cm}^{-3}$ at the photodiode junction. Bias conditions are similar to the experimental ones with a reset voltage $V_{\text{RST}} = 3.3$ V and $V_{\text{Gate}} = -0.2$ V.

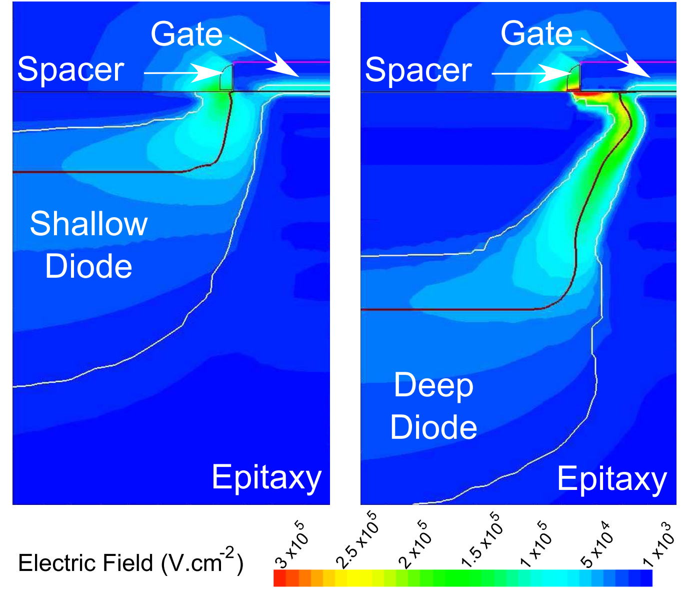

Fig. 6. TCAD simulation showing the electric field distribution into the sallow arsenic-based photodiode and the deep phosphorus-based photodiode. Bias conditions are similar to the experimental ones with a reset voltage $V_{\text{RST}} = 3.3$ V and $V_{\text{Gate}} = -0.2$ V.

The electrical simulations are performed using the Sentaurus Device software. Three electrical contacts are used: the surrounding gate, the photodiode, and the ground. To simulate the photodiode as a floating node, a reset transistor simulated in a mixed mode is added to the photodiode contact. The drain of the reset transistor is biased at the reset voltage $V_{\text{RST}} = 3.3$ V. The simulation consists of biasing the reset transistor gate from 0 to 3.3 V to reset the photodiode. Then, the reset transistor gate bias return to 0 V, allowing the photodiode to be floating. At this step, electric field distributions are analyzed. During the simulation, the following models are activated: SRH with doping dependence, band to band, and the Philips unified mobility model.

The electric field distributions into the CIS pixels during integration are presented in Fig. 6. Results highlight a high-magnitude electric field region in the deep phosphorus-based photodiode. This high-magnitude electric field region results from the overlap between the surrounding gate and the deep implantation. When exposed to TID, the induced interface traps at the gate oxide interface are probably enhanced by the local electric field as shown experimentally after the low-fluence proton irradiation in Fig. 4. Furthermore, as the TID increases, the induced positive charges trapped in the gate oxide tend to make the local electric field even more significant. This effect participates in the enhancement of the interface defect generation rate as observed experimentally in Fig. 5.

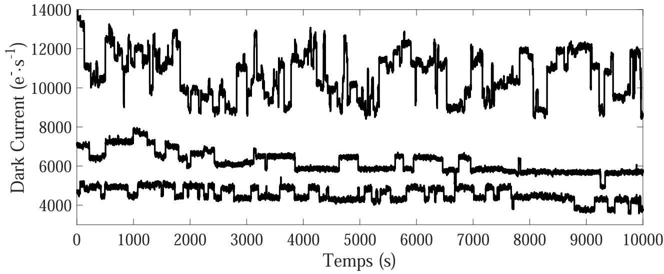

Fig. 7. Dark current fluctuations of three average pixels in the shallow arsenic-based photodiode CIS after $\phi = 10^{12}\text{cm}^{-2}$ neutron irradiation.

To summarize, the neutron irradiations have confirmed the applicability of the dark current increase prediction model in both the shallow arsenic-based photodiode CIS and the deep phosphorus-based photodiode CIS. Additionally, the proton irradiations have also confirmed the applicability of this model on the same structures. The high-magnitude electric field regions located in the overlap regions exist before irradiation in the deep phosphorus-based photodiode as proved by the TCAD simulation but can only be observed in the dark current distribution after ionizing dose absorption. For proton irradiation with TID until 1.65 krad (SiO_2), the TID dark current contribution tends to adopt a gamma-based distribution. For higher TID, the discrepancy from the prediction model can be attributed to a more complex EFE making the TID contribution the dominant source of dark current. More importantly, despite the role of the electric field linked to the TID degradation, the results give another evidence that this mixed dark current distribution model can be used in many photodiode structures and that it is independent of the doping elements. Furthermore, this experimental results highlight that the doping element (i.e., phosphorus) does not play a significant role in the radiation-induced dark current increase and its distribution.

IV. Dark Current RTS: Maximum Transition Amplitude

To compare the RTS signatures between the considered CISs, the maximum transition amplitude distribution after the neutron and proton irradiations are studied. The maximum transition amplitude distribution is a powerful tool to characterize and differentiate the RTS signatures. Indeed, the average maximum transition amplitude for the TID and the DDD contributions are $A_{\text{TID-RTS}} = 110\ \text{e}^- \cdot \text{s}^{-1}$ and $A_{\text{DDD-RTS}} = 1200\ \text{e}^- \cdot \text{s}^{-1}$, respectively. In a logscale maximum transition amplitude distribution, the two contributions are observed as two different slopes as reported in numerous articles [35]. As performed in Section III with the dark current increase, the RTS prediction model developed in [30] is used to compare the RTS maximum transition amplitude distributions of the two photodiode implantations. The investigation focuses on DDD-RTS.

A. Shallow Arsenic-Based Photodiode

Fig. 7 shows the dark current fluctuations of three average RTS pixels in the shallow arsenic-based photodiode CIS after $\phi = 10^{12}\text{cm}^{-2}$ neutron irradiation where DDD-RTS is the dominant contribution. This RTS behavior has been reported in numerous studies in CIS [24], [31], [38]. It proves that dark current fluctuations exist in arsenic-based photodiode after the neutron irradiation. Therefore, the doping element, and particularly the phosphorus element, cannot be the only responsible for the RTS in irradiated CIS.

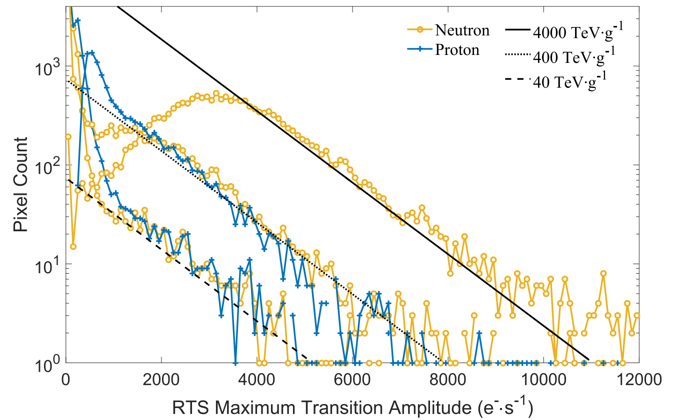

Fig. 8. RTS maximum transition amplitude distributions in the shallow arsenic-based photodiode CIS after proton and neutron irradiations. The DDD-RTS prediction model distributions accounting for displacement are plotted for the three considered DDD.

Fig. 8 shows the RTS maximum transition amplitude distributions for the shallow arsenic-based photodiode CIS after the two proton and three neutron irradiations. In the same figure, the DDD-RTS prediction model distributions accounting for displacement are plotted for the three considered DDD.

After the neutron irradiations, the RTS distributions disclose the typical slope already seen in CIS after displacement deposition, with a mean maximum transition amplitude of $A_{\text{RTS}} = 1200\ \text{e}^- \cdot \text{s}^{-1}$. For the lowest fluence, another contribution with low amplitude is observed. This contribution is usually attributed to interface defects, suggesting the existence of preirradiation and/or indirect TID-induced RTS interface defects. Finally, the applicability of the DDD-RTS prediction model is verified on the shallow arsenic-based photodiode CIS after the 22-MeV neutron irradiations.

After the proton irradiations, a frequency increase in the previously mentioned RTS interface defects contribution is observed at low RTS amplitudes (i.e., $A_{\text{TID-RTS}} = 110\ \text{e}^- \cdot \text{s}^{-1}$). As it increases with the deposited TID, it confirms the role of the interface defects in this low-amplitude contribution. Focusing on the DDD contribution, the experimental data for the two fluences are in good agreement with the DDD-RTS prediction model. Finally, the applicability of the DDD-RTS prediction model is also verified on the shallow arsenic-based photodiode CIS after the 50-MeV proton irradiations. To conclude on the shallow arsenic-based photodiode CIS, the DDD-RTS model is applicable both after the 22-MeV neutron and 50-MeV proton irradiations.

B. Deep Phosphorus-Based Photodiode

Fig. 9 shows the RTS maximum transition amplitude distribution for the deep phosphorus-based photodiode CIS after the two-proton and three-neutron irradiations.

After the neutron irradiations at the first two fluences, experimental data are in good agreement with the DDD-RTS prediction model. However, the highest fluence reveals a

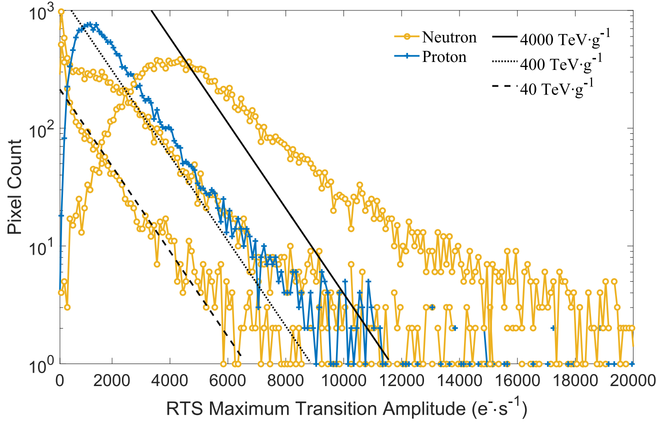

Fig. 9. RTS maximum transition amplitude distributions in the deep phosphorus-based photodiode CIS after proton and neutron irradiations. The DDD-RTS prediction model distributions accounting for displacement are plotted for the three considered DDD.

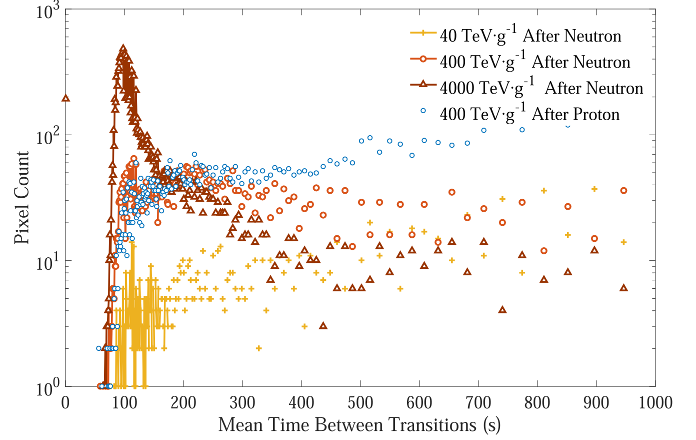

Fig. 10. Distributions of the mean time between RTS transitions for the shallow arsenic-based photodiode CIS after neutron and proton irradiations.

high discrepancy from the DDD-RTS prediction model. This discrepancy cannot be linked to a doping compensation (due to high DDD deposition [2]) or a depletion volume change as it would results in an upward shift in pixel frequency while conserving the same typical slope. Furthermore, if it were the case, the same discrepancy should have been observed in the shallow arsenic-based photodiode CIS as the depleted volume is quite similar. This discrepancy could rather be linked to high-magnitude electric field regions as highlighted in the TCAD simulation in Fig. 6. Both the indirect TID and the DDD could be at the origin of this field-assisted RTS. Contrary to pinned photodiodes, 3T photodiodes are more sensitive to TID and it is not surprising to see such degradation after 1 $krad$ (SiO_2). Moreover, from 400 to 4000 TeV $\cdot$ g^{-1}, the defects concentration into the pixels is ten times higher [39]. Hence, the probability to create displacement in high-magnitude electric field regions is higher. When located in these high-magnitude electric field regions, the DDD-induced defects with an RTS behavior could be enhanced, resulting in higher maximum transition amplitudes. Finally, the applicability of the DDD-RTS prediction model is verified in the deep phosphorus-based photodiode CIS after the 22-MeV neutron irradiations until 400 TeV $\cdot$ g^{-1}. Also, higher DDD as 4000 TeV $\cdot$ g^{-1} reveals an electric field effect proper to the pixel structure and more particularly to the overlap region.

After the lowest proton fluence, the TID-induced defects are impacted by the electric field, as shown in the dark current increase distributions in Section III. Therefore, TID-RTS is highly impacted by this electric field, making the displacement contribution invisible in the RTS maximum transition amplitude distribution and resulting in a useless observation for this study. The result for the highest fluence is reported in Fig. 9. From these experimental data, two explanations can be outlined. First, assuming that the DDD-RTS impacts a majority of pixels and becomes the dominant RTS contribution due to its higher maximum transition amplitudes, the results could show the usual DDD-RTS distribution and does not suffer from the electric field influence. Second, because of the previously mentioned electric field impact on the dark current distribution at the same fluence discussed in Section III, the observed RTS distribution could also be linked to an enhanced TID-RTS contribution. Due to this EFE already outlined in other structures [34], a clear dissociation between the TID-RTS and the DDD-RTS contributions is not possible. Finally, because of a possible electric field effect on the TID-RTS contribution, the results cannot conclude on the applicability of the DDD-RTS prediction model for the deep phosphorus-based photodiode CIS after the 50-MeV proton irradiations.

C. Conclusion on RTS Maximum Transition Amplitude

To summarize, the DDD-RTS prediction model is verified in the shallow arsenic-based photodiode CIS and the deep phosphorus-based photodiode CIS. These results give another evidence that this model can be used in many photodiode structures and that it is independent of the doping elements. Furthermore, this observation highlights that the doping element does not play a significant role in the radiation-induced RTS in CIS. Additionally, the results based on the deep phosphorus-based CIS are experimental evidence of electric field impacts on RTS after the 4000 TeV $\cdot$ g^{-1} neutron irradiation, as well as on TID-RTS when the TID is the dominant contribution. As shown by the TCAD simulation, the electric field effects can be explained by the high-magnitude electric field region under the gate present in the deep phosphorus-based photodiode CIS.

V. Dark Current RTS: Mean Time Between Transitions

The mean time between RTS transitions is studied to compare the CISs. Fig. 10 shows the distributions of the mean time between RTS transitions for the shallow arsenic-based photodiode CIS after the neutron and proton irradiations. Fig. 11 shows the distributions of the mean time between RTS transitions for the deep phosphorus-based photodiode CIS after the same neutron and proton irradiations. In both CIS, after the neutron irradiations until 400 TeV $\cdot$ g^{-1}, there is a multitude of RTS pixels with various mean time between RTS transitions. After the 4000 TeV $\cdot$ g^{-1} neutron irradiation, a majority of the RTS pixels share the same mean time

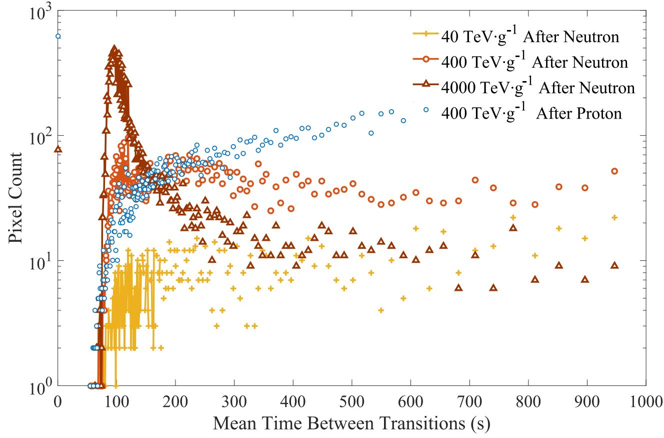

Fig. 11. Distributions of the mean time between RTS transitions for the deep phosphorus-based photodiode CIS after neutron and proton irradiations.

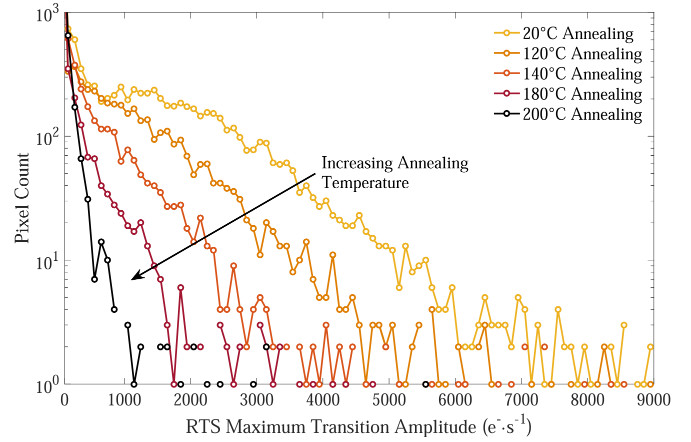

Fig. 12. Evolution of the RTS maximum transition amplitude distribution in the shallow arsenic-based photodiode CIS after 400 TeV $\cdot$ g^{-1} neutron irradiation with the annealing temperature.

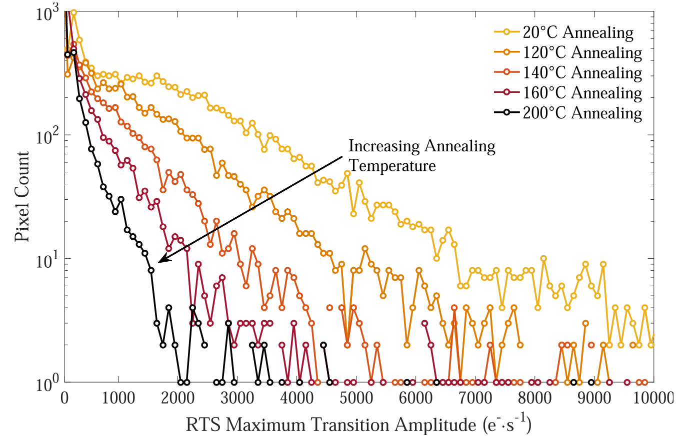

Fig. 13. Evolution of the RTS maximum transition amplitude distribution in the deep phosphorus-based photodiode CIS after 400 TeV $\cdot$ g^{-1} neutron irradiation with the annealing temperature.

between RTS transitions at 100 s. The results are similar to those reported in [40] after the proton irradiation in pinned photodiode CIS. At this fluence, the DDD-RTS is dominant as shown in the same CIS in Fig. 8. Hence, the pixel population with a mean time between RTS transitions at 100 s could be attributed to a population of DDD-RTS which seems consistent with the results based on PPD CIS in [40]. No electric field effect is observed in terms of time constant between the two lots contrary to what is observed in the maximum transition amplitude distributions. This result suggests that the electric field only impacts RTS amplitudes. The proton irradiation in both CISs tends to create more defects with high mean time between RTS transitions as observed in [40] and [41]. Finally, no major difference is observed after the 22-MeV neutron and 50-MeV proton irradiations in the mean time between RTS transitions between the shallow arsenic-based photodiode CIS and the deep phosphorus-based photodiode CIS. It gives one more evidence that the phosphorus element does not play a significant role in the radiation-induced RTS.

VI. Annealing Effects on RTS

The evolution of the RTS behavior in both CISs is studied after annealing. To avoid any electric field effect previously highlighted in Section IV, the investigations are led on the CIS referred to as D and I, which have been irradiated with neutron at 400 TeV $\cdot$ g^{-1}. Eight 30-min annealing treatments are considered ranging from 80 °C to 200 °C with a 20 °C step. The evolution of the maximum transition amplitude distribution with the annealing temperature is reported in Figs. 12 and 13 for the shallow arsenic-based photodiode CIS and the deep phosphorus-based CIS, respectively. The reduction of the RTS amplitude distribution frequency with increasing annealing temperature is observed for both CISs. Moreover, for both CISs, the slope of the RTS amplitude distribution increases with annealing temperature. The typical slope with the mean maximum transition amplitude of $A_{\text{RTS}} = 1200$ e$^{-} \cdot$ s^{-1}, which has been verified in Section IV, is only visible after irradiation (i.e., 20 °C). The annealing treatments tend to recover the DDD-induced RTS centers and to reduce their maximum transition amplitudes leading to a global reduction of the RTS amplitude distribution. These effects are visible in the shallow arsenic-based photodiode CIS as well as in the deep phosphorus-based CIS, suggesting that the photodiode doping element does not play a major role in the RTS maximum transition amplitude evolution with annealing.

Fig. 14 shows the evolution of the number of RTS pixels in the shallow arsenic-based photodiode CIS and the deep phosphorus-based CIS after the 400 TeV $\cdot$ g^{-1} neutron irradiation with the annealing temperature. For both sensors, a marked reduction in the number of RTS pixels is observed around 100 °C. For higher annealing temperatures, the RTS pixel reduction becomes less and less effective as the temperature increases. The same RTS pixel reduction with annealing temperature has been observed in proton-irradiated CCD in [42] and in neutron-irradiated CIS in [39]. Moreover, it corresponds to the typical annealing behavior of clusters responsible for the dark current in irradiated imagers [8]. This result suggests that this RTS pixel reduction with annealing temperature is a common mechanism in irradiated image sensors, suggesting similarities in the DDD-induced defects recovering dynamic. As discussed in [18], the observed annealing behaviors mostly lie in the reduction of amorphous inclusions. The required thermal energy certainly depends on the geometry and the stability of the clusters which varies from cluster to cluster.

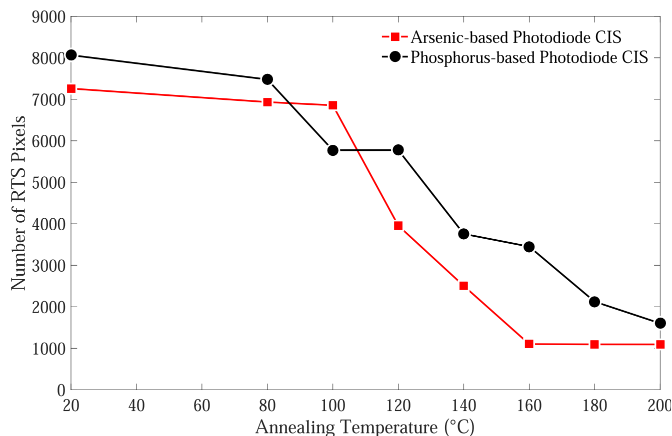

Fig. 14. Evolution of the number of RTS pixels in the shallow arsenic-based photodiode CIS and the deep phosphorus-based CIS after 400 TeV $\cdot$ g^{-1} neutron irradiation with the annealing temperature.

Due to the variety of thermal relaxation processes available, the annealing gradually reduces the electrical effects of clusters by recovering defect states. Such processes account for the annealing observed in a large range of temperatures between 100 °C and 160 °C which differs from sharp annealing which would account for the recovering of a specific impurity complex.

VII. Discussion

Many defects in silicon have been identified to be metastable or bistable [43] and are, therefore, susceptible to behave as RTS centers. However, many of them have shallow energy level and are, therefore, not good candidates to act as high-rate generation centers. Indeed, mid-gap defects are more likely to be high-rate generation centers even if the cross sections for generated electrons and holes are also prominent parameters [9]. Moreover, the temperature stability of possible RTS centers must be consistent with the experimental observations. Despite its multistability [15], the divacancy cannot be the only responsible for the RTS behavior. Impurity– and dopant–vacancy complexes appear also to be good candidates regarding their multiple potential wells (i.e., configurations and charge states) and their temperature stability, which are consistent with experimental results [14], [44]. Among them, the P–V center and other vacancy–oxygen complex defects [45] seem to be good candidates. Even if the multistability of these defects is proven, their role in the observed RTS behavior present in irradiated devices is by no means certain. Experimental results show a huge diversity in the RTS behavior and these defects seem inconsistent with multilevel RTS centers reaching sometimes more than five levels and RTS amplitudes of several thousands of electrons per second [24], [31].

It is also important to have in mind that most of the isolated defect characterization studies are based on electron irradiations aiming to produce small displacement damage into the silicon. Unlike electrons, the proton and neutron irradiations are known to produce cascades of defects [26]. Based on the presented results, it is tentatively concluded that RTS defects are more likely to be associated with intrinsic silicon defect clusters rather than impurity- or dopant-related defects. The possibility of participation of impurities, doping elements, and, when applicable, the phosphorus, in the dark current and the RTS is not eliminated, and interactions of these defects within a cluster are not ruled out. Moreover, possible field-assisted mechanisms could also have an impact on RTS centers [34]. This observation making intrinsic silicon defect clusters the principal sources of degradations after irradiation can be extended to other silicon-based devices including CCD, CIS, and SPAD and could explain the similarities with variable retention time (VRT) in memories reported in [46]. The use of electron irradiations with a production of isolated defects for the investigation of RTS in CIS as initiated in [47] could be a promising way to link the commonly observed RTS after the proton or neutron irradiations and the electrical behavior of isolated defects measured by DLTS and EPR.

VIII. Conclusion

Radiation-induced effects after the 22-MeV neutron and 50-MeV proton irradiations on the shallow arsenic-based photodiode CIS and the deep phosphorus-based photodiode CIS have been investigated, highlighting the applicability of the same dark current increase and RTS maximum transition amplitude models. Such analytic tools have been verified on other photodiode structures in past studies, and these results further extend their universality. Moreover, no significant difference has been observed in the mean time between RTS transitions in the shallow arsenic-based CIS and the deep phosphorus-based photodiode CIS. These results confirm that the phosphorus doping element does not play a significant role either on the dark current increase, in the dark current RTS maximum transition amplitude, or in the mean time between RTS transitions. Furthermore, investigations on the RTS behavior evolution with annealing does not lead to any clear difference between the shallow arsenic-based CIS and the deep phosphorus-based photodiode CIS. The results after annealing reveal the same recovery dynamic in irradiated CCD and CIS, suggesting that the phosphorus doping element does not play a significant role after annealing. Therefore, this work is a piece of experimental evidence supporting the idea that DDD-induced RTS in silicon-based devices is principally due to defect clusters mainly constituted of intrinsic silicon defects (i.e., clusters of vacancies and interstitials) [18], [25]–[27]. As observed for the dark current, phosphorus atoms, when present, could possibly participate in the global RTS behavior but are not the main contributor.

IX. Disclaimer

This publication reflects the views only of the authors, and Fusion for Energy cannot be held responsible for any use which may be made of the information contained therein.

References

[1] T. R. Oldham and F. B. McLean, “Total ionizing dose effects in MOS oxides and devices,” *IEEE Trans. Nucl. Sci.*, vol. NS-50, no. 3, pp. 483–499, Jun. 2003.

[2] J. R. Srour and J. W. Palko, “A framework for understanding displacement damage mechanisms in irradiated silicon devices,” *IEEE Trans. Nucl. Sci.*, vol. NS-53, no. 6, pp. 3610–3620, Dec. 2006.

[3] W. Shockley and W. T. Read, “Statistics of the recombinations of holes and electrons,” *Phys. Rev.*, vol. 87, no. 5, pp. 835–842, Sep. 1952.

[4] J. R. Srour and D. H. Lo, "Universal damage factor for radiation-induced dark current in silicon devices," *IEEE Trans. Nucl. Sci.*, vol. NS-47, no. 6, pp. 2451–2459, Dec. 2000.

[5] J. R. Srour, R. A. Hartmann, and S. Othmer, "Transient and permanent effects of neutron bombardment on a commercially available N-buried-channel CCD," *IEEE Trans. Nucl. Sci.*, vol. NS-27, no. 6, pp. 1402–1410, Dec. 1980.

[6] C. Marshall *et al.*, "Hot pixel annealing behavior in CCDs irradiated at-84°C," *IEEE Trans. Nucl. Sci.*, vol. NS-52, no. 6, pp. 2672–2677, Dec. 2005.

[7] M. Raine *et al.*, "Exploring the kinetics of formation and annealing of single particle displacement damage in microvolumes of silicon," *IEEE Trans. Nucl. Sci.*, vol. NS-61, no. 6, pp. 2826–2833, Dec. 2014.

[8] G. R. Hopkinson and A. Mohammadzadeh, "Comparison of ccd damage due to 10- and 60-mev protons," *IEEE Trans. Nucl. Sci.*, vol. NS-50, no. 6, pp. 1960–1967, Dec. 2003.

[9] J. Bourgoin and M. Lannoo, *Point Defects in Semiconductors II: Experimental Aspects*. New York, NY, USA: Springer-Verlag, 1983.

[10] M. S. Robbins, "High-energy proton-induced dark signal in silicon charge coupled devices," *IEEE Trans. Nucl. Sci.*, vol. NS-47, no. 6, pp. 2473–2479, Dec. 2000.

[11] J.-M. Belloir *et al.*, "Dark current spectroscopy on alpha irradiated pinned photodiode CMOS image sensors," *IEEE Trans. Nucl. Sci.*, vol. NS-63, no. 4, pp. 2183–2192, Aug. 2016.

[12] J.-M. Belloir *et al.*, "Dark current spectroscopy in neutron, proton and ion irradiated CMOS image sensors: From point defects to clusters," *IEEE Trans. Nucl. Sci.*, vol. NS-64, no. 1, pp. 27–37, Jan. 2017.

[13] A. Le Roch *et al.*, "Radiation-induced defects in 8T-CMOS global shutter image sensor for space applications," *IEEE Trans. Nucl. Sci.*, vol. NS-65, no. 8, pp. 1645–1653, Aug. 2018.

[14] G. D. Watkins and J. W. Corbett, "Defects in irradiated silicon: Electron paramagnetic resonance and electron-nuclear double resonance of the Si-*E* center," *Phys. Rev.*, vol. 134, no. 5A, pp. A1359–A1377, Jul. 1964.

[15] G. D. Watkins and J. W. Corbett, "Defects in irradiated silicon: Electron paramagnetic resonance of the divacancy," *Phys. Rev.*, vol. 138, no. 2A, pp. A543–A555, Apr. 1965.

[16] J. Kreissl, M. Hoehne, and W. Gehlhoff, "Identification of diluted small defect clusters in silicon by electron paramagnetic resonance," *Zeitschrift für Physik D At., Molecules Clusters*, vol. 20, nos. 1–4, pp. 373–375, Mar. 1991.

[17] M. Moll, H. Feick, E. Fretwurst, G. Lindström, and C. Schütze, "Comparison of defects produced by fast neutrons and ^{60}Co-gammas in high-resistivity silicon detectors using deep-level transient spectroscopy," *Nucl. Instrum. Meth. Phys. Res. A, Accel. Spectrom. Detect. Assoc. Equip.*, vol. 388, no. 3, pp. 335–339, Apr. 1997.

[18] J. W. Palko and J. R. Srour, "Amorphous inclusions in irradiated silicon and their effects on material and device properties," *IEEE Trans. Nucl. Sci.*, vol. NS-55, no. 6, pp. 2992–2999, Dec. 2008.

[19] P. W. Marshall, C. J. Dale, E. A. Burke, G. P. Summers, and G. E. Bender, "Displacement damage extremes in silicon depletion regions," *IEEE Trans. Nucl. Sci.*, vol. NS-36, no. 6, pp. 1831–1839, Dec. 1989.

[20] G. R. Hopkinson, "Cobalt60 and proton radiation effects on large format, 2-D, CCD arrays for an Earth imaging application," *IEEE Trans. Nucl. Sci.*, vol. NS-39, no. 6, pp. 2018–2025, Dec. 1992.

[21] I. H. Hopkins and G. R. Hopkinson, "Random telegraph signals from proton-irradiated CCDs," *IEEE Trans. Nucl. Sci.*, vol. NS-40, no. 6, pp. 1567–1574, Dec. 1993.

[22] I. H. Hopkins and G. R. Hopkinson, "Further measurements of random telegraph signals in proton irradiated CCDs," *IEEE Trans. Nucl. Sci.*, vol. NS-42, no. 6, pp. 2074–2081, Dec. 1995.

[23] T. Nuns, G. Quadri, J.-P. David, O. Gilard, and N. Boudou, "Measurements of random telegraph signal in CCDs irradiated with protons and neutrons," *IEEE Trans. Nucl. Sci.*, vol. NS-53, no. 4, pp. 1764–1771, Aug. 2006.

[24] G. R. Hopkinson, V. Goiffon, and A. Mohammadzadeh, "Random telegraph signals in proton irradiated CCDs and APS," *IEEE Trans. Nucl. Sci.*, vol. NS-55, no. 4, pp. 2197–2204, Aug. 2008.

[25] K. Gill, G. Hall, and B. MacEvoy, "Bulk damage effects in irradiated silicon detectors due to clustered divacancies," *J. Appl. Phys.*, vol. 82, no. 1, pp. 126–136, Jul. 1997.

[26] J. R. Srour and J. W. Palko, "Displacement damage effects in irradiated semiconductor devices," *IEEE Trans. Nucl. Sci.*, vol. NS-60, no. 3, pp. 1740–1766, Jun. 2013.

[27] A. Jay *et al.*, "Simulation of single particle displacement damage in silicon–Part II: Generation and long-time relaxation of damage structure," *IEEE Trans. Nucl. Sci.*, vol. NS-64, no. 1, pp. 141–148, Jan. 2017.

[28] F. Di Capua *et al.*, "Random telegraph signal in proton irradiated single-photon avalanche diodes," *IEEE Trans. Nucl. Sci.*, vol. NS-65, no. 8, pp. 1654–1660, Aug. 2018.

[29] B. Pain and B. R. Hancock, "Accurate estimation of conversion gain and quantum efficiency in CMOS imagers," *Proc. SPIE*, vol. 5017, pp. 94–103, May 2003.

[30] V. Goiffon, G. R. Hopkinson, P. Magnan, F. Bernard, G. Rolland, and O. Saint-Pe, "Multilevel RTS in proton irradiated CMOS image sensors manufactured in a deep submicron technology," *IEEE Trans. Nucl. Sci.*, vol. NS-56, no. 4, pp. 2132–2141, Aug. 2009.

[31] C. Durnez, V. Goiffon, C. Virmontois, J.-M. Belloir, P. Magnan, and L. Rubaldo, "In-depth analysis on radiation induced multi-level dark current random telegraph signal in silicon solid state image sensors," *IEEE Trans. Nucl. Sci.*, vol. NS-64, no. 1, pp. 19–26, Jan. 2017.

[32] C. Virmontois *et al.*, "Similarities between proton and neutron induced dark current distribution in CMOS image sensors," *IEEE Trans. Nucl. Sci.*, vol. NS-59, no. 4, pp. 927–936, Aug. 2012.

[33] J.-M. Belloir *et al.*, "Pixel pitch and particle energy influence on the dark current distribution of neutron irradiated CMOS image sensors," *Opt. Express*, vol. 24, no. 4, pp. 4299–4315, Feb. 2016.

[34] A. Le Roch *et al.*, "Radiation-induced leakage current and electric field enhancement in CMOS image sensor sense node floating diffusions," *IEEE Trans. Nucl. Sci.*, vol. NS-66, no. 3, pp. 616–624, Mar. 2019.

[35] V. Goiffon, "Radiation effects on CMOS active pixel image sensors," in *Ionizing Radiation Effects in Electronics: From Memories to Imagers*, Boca Raton, FL, USA: CRC Press, 2015, pp. 295–332.

[36] V. Goiffon *et al.*, "Radiation damages in CMOS image sensors: Testing and hardening challenges brought by deep sub-micrometer CIS processes," *Proc. SPIE*, vol. 7826, Oct. 2010, Art. no. 78261S.

[37] J. Bogaerts, B. Dierickx, and R. Mertens, "Enhanced dark current generation in proton-irradiated CMOS active pixel sensors," *IEEE Trans. Nucl. Sci.*, vol. NS-49, no. 3, pp. 1513–1521, Jun. 2002.

[38] C. Virmontois *et al.*, "Dark current random telegraph signals in solid-state image sensors," *IEEE Trans. Nucl. Sci.*, vol. NS-60, no. 6, pp. 4323–4331, Dec. 2013.

[39] C. Virmontois *et al.*, "Total ionizing dose versus displacement damage dose induced dark current random telegraph signals in CMOS image sensors," *IEEE Trans. Nucl. Sci.*, vol. NS-58, no. 6, pp. 3085–3094, Dec. 2011.

[40] C. Virmontois *et al.*, "Radiation-induced dose and single event effects in digital CMOS image sensors," *IEEE Trans. Nucl. Sci.*, vol. NS-61, no. 6, pp. 3331–3340, Dec. 2014.

[41] V. Goiffon, P. Magnan, P. Martin-Gonthier, C. Virmontois, and M. Gaillardin, "Evidence of a novel source of random telegraph signal in CMOS image sensors," *IEEE Electron Device Lett.*, vol. 32, no. 6, pp. 773–775, Jun. 2011.

[42] T. Nuns, G. Quadri, J.-P. David, and O. Gilard, "Annealing of proton-induced random telegraph signal in CCDs," *IEEE Trans. Nucl. Sci.*, vol. NS-54, no. 4, pp. 1120–1128, Aug. 2007.

[43] B. N. Mukashev, K. A. Abdullin, and Y. V. Gorelkinskii, "Metastable and bistable defects in silicon," *Physics-Uspekhi*, vol. 43, no. 2, pp. 139–150, Feb. 2000.

[44] E. L. Elkin and G. D. Watkins, "Defects in irradiated silicon: Electron paramagnetic resonance and electron-nuclear double resonance of the Arsenic- and antimony-vacancy pairs," *Phys. Rev.*, vol. 174, no. 3, pp. 881–897, Oct. 1968.

[45] T. Umeda *et al.*, "Single silicon vacancy-oxygen complex defect and variable retention time phenomenon in dynamic random access memories," *Appl. Phys. Lett.*, vol. 88, no. 25, Jun. 2006, Art. no. 253504.

[46] V. Goiffon *et al.*, "Radiation-induced variable retention time in dynamic random access memories," *IEEE Trans. Nucl. Sci.*, vol. NS-67, no. 1, pp. 234–244, Jan. 2020.

[47] A. Le Roch *et al.*, "Comparison of X-ray and electron radiation effects on dark current non-uniformity and fluctuations in CMOS image sensors," *IEEE Trans. Nucl. Sci.*, vol. NS-67, no. 1, pp. 268–277, Jan. 2020.